

Facile Synthesis and Optical Properties of Rod-like Copper Oxide Nanoparticles

Moges Tsega Yihunie

Department of Physics, College of Science, Bahir Dar University, Bahir Dar 600079, Ethiopia.

e-mail: mogestsega@yahoo.com

IMPRESS

Abstract: Copper oxide (CuO) nanoparticles (NPs) were synthesized by the sol-gel method, followed by calcination at 600 °C for 2 h. The XRD pattern indicated that the synthesized CuO NPs had a monoclinic structure, with an average crystallite size of 53 nm. The FT-IR spectra showed that surfactant molecules were adsorbed on the surface of the CuO nanoparticles, along with the presence of Cu-O bonding. The TEM analysis revealed rod-like CuO NPs with diameters of about 50 nm and lengths ranging from 150 to 200 nm. The XPS analysis confirmed that copper and oxygen were synthesized as the main components with Cu²⁺ and O²⁻ oxidation states. The optical band gap of CuO was calculated to be 2.0 eV. The maximum PL emission was recorded at 430 nm for the 365 nm excitation wavelength, and the change in PL intensity and peak shift was calculated as a function of excitation wavelength. Reflectance spectra show increasing reflectance with wavelength, while Mie calculations indicate decreasing spectral efficiencies, along with a reduction in the real refractive index and an increase in the imaginary part. A slight size-dependent enhancement in optical response is also observed.

Keywords: CuO, nanoparticles, sol-gel, photoluminescence, Mie analysis.

1. INTRODUCTION

Nanoparticles and nanostructured materials are currently gaining popularity due to their high surface-area-to-volume ratio [1, 2]. Metal oxide nanoparticles (NPs) have remarkable optical, electrical, magnetic, catalytic, and biological capabilities due to their distinct physical and chemical properties that differ greatly from those of the bulk metal [1, 3]. CuO NPs are the most abundant transition metal oxide binary compound, as well as the most chemically and physically stable. It has a monoclinic structure and a narrow bandgap of 1.3–1.7 eV with *p*-type semiconductor material [4]. The multivalent states of CuO NPs also have interesting physicochemical properties. CuO NPs were of great interest due to their potential applications in a wide variety of areas, including electronic and optoelectronic devices, such as lithium-ion batteries, photocatalytic activities, gas sensors, biomedical applications, photovoltaics, and supercapacitor materials [5–10]. CuO NPs, with their extensive redox reactions and coloring effects, can alter optical characteristics and up-conversion [11]. CuO has also been employed as a photocatalyst and host material for various luminous emissions [11]. Recently, researchers explored the optical properties of CuO nanostructures [12–14]. However, a report on the luminescence property is limited. The properties of CuO NPs highly depend on their synthesis methods [15]. The synthesis methods of CuO NPs can control particle size, morphology, and crystallinity.

CuO NPs were prepared using a variety of processes, including sol-gel [16], solution-combustion method [6], ball milling [7], precipitation [14], hydrothermal [17], chemical bath deposition [18], solid-state [19], and green synthesis [20]. Of these methods, the sol-gel method is straightforward, suitable for mass production, achieves relatively low temperatures and ambient conditions, and is an economical solution-based growth technology. This method, which regulates precursor concentrations, reaction time, and temperature, is especially suitable for high-quality crystal formation, a greater surface area, and a wide range of shape. Despite the extensive literature on the synthesis of CuO nanostructures via solution-based methods, the systematic investigations linking sol-gel synthesis conditions to the photoluminescence (PL) behavior of CuO nanoparticles is not fully understood. This study presents the optimized and controlled sol-gel synthesis of CuO NPs to study its structural, morphological, and optical properties.

2. EXPERIMENTAL DETAILS

All the reagents used in this chemical synthesis were supplied without any further purification. For the synthesis of CuO NPs, 0.97 g of cupric nitrate trihydrate ($\text{Cu}(\text{NO}_3)_2 \cdot 3\text{H}_2\text{O}$) was dissolved in 25 mL of DI water. This solution was kept under vigorous stirring for 3 h at room temperature. During this stirring, 0.456 g of citric acid dissolved in 10 mL DI water was added dropwise. The resulting solution was kept in the oven at 125 °C for 3 h. The dried gel was then calcined at 600 °C for 2 h in the muffle furnace and collected for further characterization.

The crystal structure of the samples was determined by powder X-ray diffraction (XRD, Bucker D8 Advance) using $\text{Cu K}\alpha$ ($\lambda = 1.5418 \text{ \AA}$) radiation. The transmittance property of CuO was studied using Perkin Elmer Spectrum 100 Fourier transformed infrared spectroscopy (FTIR). Morphology and lattice diffraction analyses were carried out using a transmission electron microscope (TEM; JEOL, JEM-2010F) operating at a 200 kV accelerating voltage. The oxidation states of the synthesized CuO NPs were determined using X-ray photoelectron spectroscopy (XPS) with a PHI 5400 XPS spectrometer using a monochromatic $\text{Al K}\alpha$ X-ray source (1486.6 eV, 15 kV, 300 W) and a hemispherical sector analyzer. The reflectance UV-vis spectrum was obtained using a Shimadzu UV-3600 spectrometer with an integrating sphere. PL spectra of the synthesized CuO NPs were recorded at room temperature on a fluorescence spectrophotometer (F-7000) using a 150 W xenon lamp as an excitation source and a grating to select a suitable wavelength for excitation.

3. RESULTS AND DISCUSSION

3. 1. Structural Analysis

The XRD spectrum of the synthesized CuO NPs is illustrated in Fig. 1. The diffraction peaks observed at 2θ are attributed to the (110), (002), (111), (-112), (-202), (020), (202), (-113), (-311), (320), (311), and (222) planes associated with the monoclinic structure of CuO NPs. This result is consistent with prior reports [5, 21, 22]. The observed XRD pattern also matches the standard JCPDS Card no. 45-0937 of the pure CuO phase [23, 24]. The Miller-indexed (002) and (111) reflections were the strongest, suggesting that the NPs produced by the sol-gel method have preferred crystal planes. The sharp and highly intense diffraction peaks in the XRD profile indicate that the CuO NPs are highly crystalline. In addition, no impurities were noticed. Thus, the XRD pattern strongly supports the formation of CuO nanoparticles.

The average crystallite size (D) was calculated from the XRD pattern using Scherrer's equation [25]:

$$D = \frac{0.9\lambda}{\beta \cos\theta} \quad (1)$$

The dislocation density (δ), which gives the number of defects in a crystal, and the micro-strain (ε) were determined using the following relations [14]:

$$\delta = \frac{1}{D^2} \quad (2)$$

$$\varepsilon = \frac{\beta}{4 \tan \theta} \quad (3)$$

The lattice constants ($a \neq b \neq c$) and unit cell volume (V) are also calculated from the strong diffraction peaks of the (002), (111), and (-202) planes in the case of the monoclinic crystal [26] using

$$\frac{1}{(d_{hkl})^2} = \frac{1}{\sin^2 \gamma} \left(\frac{h^2}{a^2} + \frac{k^2 \sin^2 \gamma}{b^2} + \frac{l^2}{c^2} - \frac{2hl \cos \gamma}{ac} \right) \quad (4)$$

$$V = abc \sin \gamma \quad (5)$$

where λ is the wavelength of the X-ray used, which is CuK α radiation ($\lambda = 1.5406 \text{ \AA}$), β is the full width at half maximum (in radians), and θ is the Bragg's angle, where a , b , and c are the lattice constants, d_{hkl} is the interplanar distance, γ is the interfacial angle ($\gamma = 99.41^\circ$), and h , k , and l are the Miller indices. The calculated average crystallite size is found to be 53 nm, as shown in Table 1. Table 1 also displays the results for peak position and estimated structural parameters. The obtained dislocation density is $3.6 \times 10^{14} \text{ m}^{-2}$ and the micro-strain is 8.3×10^{-3} . The calculated lattice parameters were $a = 4.6336 \text{ \AA}$, $b = 3.4296 \text{ \AA}$, and $c = 5.1251 \text{ \AA}$, and the unit cell volume was 80.33 \AA^3 which is in good agreement with previous reports [6, 14, 17].

3.2 . FT-IR spectroscopy

FT-IR spectroscopy is an important instrument for identifying the presence of various functional groups in the synthesized powder. Figure 2 shows the FTIR spectrum of CuO NPs. The band at 3400 cm^{-1} corresponds to the O–H hydroxyl group stretching vibration [27]. This O–H vibration arises from hydrogen bonding between CuO and adsorbed water molecules, as well as interactions with their surfaces, indicating that the surface of the NPs absorbs water from the environment. Peaks in the range of $2100\text{--}2600 \text{ cm}^{-1}$ may be associated with C \equiv C stretching vibrations or the adsorption of CO $_2$ on the surface of CuO NPs [28]. The vibration band at 1800 cm^{-1} is attributed to the C=O stretching mode [27]. The band at 1600 cm^{-1} can be attributed to the Cu–O stretching vibration, confirming the formation of CuO

NPs [29]. The weak peak at 1350 cm^{-1} usually appears in the spectrum and denotes the C–H stretching mode. The peak at 1050 cm^{-1} is due to O–H bending and C–O and O–Cu pair stretching [30].

3.3 . Microstructure

The particle size and morphology of the sample are analyzed by transmission electron microscopy (TEM). Figure 3 (a) displays a picture of the calcined powder. The black color of the CuO product is clearly visible. Figures 3 (b) and 3 (c) show the TEM images of the prepared CuO NPs at different magnifications, allowing for a more detailed investigation of their structural features. These images showed how NPs get agglomerated and have irregular forms [31, 32]. Two distinct particle shapes: spherical and rod were shown by TEM images. The rod-shaped particles had a diameter of roughly 50 nm and a length of 150–200 nm. The majority of nanoparticles detected in the micrographs are roughly spherical, with a small number of elongated particles. The particle size of a spherical morphology was in the range of 50–60 nm, which is in good agreement with the calculated crystallite size in the Scherrer formula. Figure 3 (d) depicts the selected area electron diffraction (SAED) pattern of CuO NPs. The diffraction rings are indexed as (002), (111), and (-202) planes, confirming the formation of the polycrystalline monoclinic crystal of the synthesized CuO NPs [14, 33]. The TEM study also supports the XRD result.

3.4 . XPS analysis

The chemical oxidation state of the CuO NPs was investigated by X-ray photoelectron spectroscopy (XPS), and the results are presented in Fig. 4. The peaks of the XPS survey spectrum in Fig. 4 (a) indicated the presence of Cu, O, and C (used as references) elements in the synthesized CuO NPs [5]. Other contaminants did not show up as clearly on the survey scan. As seen in Fig. 4(b), the XPS spectrum for the Cu 2p core level displays two peaks at 934 eV and 953.9 eV, which correspond to Cu 2p_{3/2} and Cu 2p_{1/2}, respectively. The distance between Cu 2p_{3/2} and Cu 2p_{1/2} was measured to be 19.9 eV, indicating the presence of Cu²⁺ ions in the synthesized NPs [34]. The presence of the Cu²⁺ chemical state was confirmed by the detection of two additional satellite peaks at 943.6 and 962.5 eV in addition to the Cu 2p peaks. Figure 4 (c) shows the O1s spectrum of CuO NPs. The O1s spectrum is now deconvoluted into distinct components, where the lower binding energy peak at ~529.9 eV corresponds to lattice oxygen (O²⁻) in CuO, while the higher binding energy component at ~532.1 eV is assigned to surface hydroxyl groups and/or adsorbed water molecules [35, 36]. This result is in agreement with the previous reports [37, 38].

3.5 . Optical properties

Figure 5 (a) depicts the diffuse reflectance spectrum of CuO NPs recorded at room temperature in the range of 200–800 nm. The sample is extremely reflective in the visual region, as indicated in the Fig. 5 (a) [12]. A significant absorption edge is found at around 354 nm, which is consistent with previous reports for CuO NPs [39, 40]. The reflectance data was converted to the absorption coefficient $F(R)$ values using the Kubelka-Munk equation [41]:

$$\alpha = F(R) = \frac{(1-R)^2}{2R} \quad (6)$$

where $F(R)$ is the Kubelka–Munk function, α is the absorption coefficient, and R is the reflectance (%). The band gap energy (E_g) of the CuO NPs was evaluated using Tauc's plot in accordance with the equation [42]:

$$\alpha h\nu = A(h\nu - E_g)^n \quad (7)$$

where $h\nu$ represents the photon energy, A is a proportionality constant, E_g is the bandgap energy, and n is the exponential constant index, which depends on the nature of the transition ($n = 2$ for an indirect allowed transition). Figure 5 (b) depicts the Tauc plot of $(\alpha h\nu)^{1/2}$ vs. $h\nu$, which is based on the indirect transition. The energy band gap is calculated by extrapolating a line tangent to the $h\nu$ axis. The estimated optical energy band gap was approximately 2.0 eV, indicating its potential in photocatalysis. This value and the reported values agree quite well [14, 43]. However, the obtained E_g value for synthesized CuO NPs is substantially higher than that of bulk CuO (1.85 eV) [44, 45] but lower than previously reported values [24, 46, 47]. The quantum confinement effect brought on by the nanosized crystals found in TEM examination is responsible for the high E_g value [47].

One useful method for examining the atomic structure of a crystal is optical conductivity. The optical response of a material is mainly studied in terms of the optical conductivity (σ), which is given by the relation [48]:

$$\sigma = \frac{\alpha nc}{4\pi} \quad (8)$$

where c is the velocity of light, α is the absorption coefficient, and n is the refractive index. The optical conductivity of CuO NPs as a function of photon energy is displayed in Fig. 5(c). Optical conductivity generally increases with photon energy because higher-energy photons can excite electrons across larger energy gaps and into higher conduction states,

thereby enhancing the material's ability to absorb and transport optical energy. This trend is often consistent with the decrease in reflectance at higher photon energies, since more photons are absorbed rather than reflected, leading to stronger electronic transitions [49]. The Urbach energy can also be calculated using [50]:

$$\alpha = \alpha_0 e^{\frac{h\nu}{E_U}} \quad (9)$$

where α is the absorption coefficient, α_0 is a constant, $h\nu$ is the incident photon energy, and E_U is the Urbach energy, which indicates the width of the band tails of the localized states in the gap region and is used to characterize the degree of disorder in crystalline solids. Fig. 5(d) shows $\text{Ln}\alpha$ as a function of photon energy $h\nu$. Urbach energy is derived from the inverse of the slope of $\text{Ln}\alpha$ vs $h\nu$. The slope was calculated to be 0.18. The computed Urbach energy value of CuO NPs was 5.56 eV [48, 51], which is higher than that of other metal oxides. The Urbach energy, which characterizes the width of the exponential absorption tail near the band edge, provides insight into the degree of disorder and defect states in the material. A larger Urbach energy indicates more localized states that facilitate sub-bandgap absorption, while at higher photon energies the optical conductivity dominates as band-to-band transitions become more pronounced. Thus, the interplay between optical conductivity, reflectance, and Urbach energy highlights how intrinsic electronic structure and disorder collectively govern the material's optical response.

Figure 6 shows the PL emission spectra of CuO NPs recorded at room temperature with excitation wavelengths of 325, 340, and 365 nm. Every spectrum has an emission peak that is easily seen. Violet emission peaks are visible in the spectra at 428, 428.6, and 430.4 nm at excitation wavelengths of 325, 340, and 365 nm, respectively. The plot indicates that as the excitation wavelength increases, the emission's intensity rises linearly. The excitation source at 365 nm produced the greatest emission peak. Emission intensity rises with increasing excitation wavelength because the unrelaxed photoexcited species separate from the lower-energy excited species more clearly [52]. The increase in emission intensity at higher excitation wavelengths was consistent with the findings of I. Abdullahi et al. [11]. A high recombination rate is indicated by the strong band. Conversely, a decrease in peak heights suggests that band levels are easily accessible for electron migration and that electron-hole couples are well separated [33]. The intensity shift was attributed to radiative recombination caused by surface defect passivation [53]. The recombination process involves moving the electron back to the valence band while simultaneously emitting energy. The luminescence bands in the violet region (428–430 nm) may be attributed to the band edge emission or defect levels in CuO caused by oxygen

vacancy and Cu interstitial [12, 54]. Additionally, the violet emission peak is a result of the charge transfer transition from Cu and O ions in the CuO lattices [55]. The emission peaks are also slightly red-shifted, which is directly linked to the average grain size. Because 365 nm light has less energy than 320 nm and 340 nm light, the spectra show a significant red shift when compared to those excited at lower wavelengths. In general, visible emissions are strongly dependent on the synthesis conditions, nanoparticle size, and shape. The PL value achieved here is consistent with previous reports [54, 56].

3.6 . Mie analysis

The optical properties of spherical nanoparticles can also be studied using the Mie theory [58]. In Mie scattering theory, optical scattering efficiency (Q_{sca}) and extinction efficiency (Q_{ext}) [58] can be calculated using

$$Q_{sca} = \frac{2}{x^2} \sum_{n=1}^{\infty} (2n+1) (|a_n|^2 + |b_n|^2)$$

$$Q_{ext} = \frac{2}{x^2} \sum_{n=1}^{\infty} (2n+1) \text{Re}(a_n + b_n)$$
(10)

where $x = \frac{2\pi r}{\lambda}$ is the size parameter, r is the radius of the nanoparticle, a_n and b_n are the Mie scattering coefficients,

which are calculated numerically. For a simpler analysis, the directional scattering behavior can be described by the average cosine of the scattering angle, known as the asymmetry factor (g) [59], given by

$$g = \langle \cos \theta \rangle = \frac{\int_0^{\pi} 2\pi S_{11}(\theta) \cos \theta \sin \theta d\theta}{\int_0^{\pi} 2\pi S_{11}(\theta) \sin \theta d\theta}$$
(11)

where $S_{11}(\theta)$ is the scattering matrix and θ is the scattering angle. The efficiency factors Q_{sca} , Q_{ext} , Q_{abs} , the real and imaginary (n , k) index of refractions, and the asymmetry (g) were determined using the Mie scattering theory with the help of Mie Plot v.4.3 software. The changes in optical characteristics for particle size of 50, 60, and 70 nm are shown in Fig. 7. The optical characteristics of CuO nanoparticles exhibit a clear dependence on both wavelength and particle size. With increasing wavelength, the scattering efficiency, and extinction efficiency display a decreasing trend with wavelength, reflecting the reduced contribution of scattering and attenuation in this spectral region (Figs. 7(a) and 7(b)). As wavelength increases (lower photon energy), fewer electronic transitions are excited, so the polarization response weakens, and the real index decreases (Fig. 7(d)). When considering particle size within the 50–70 nm range, both

extinction efficiency and scattering efficiency increase with increasing nanoparticle diameter. This size-dependent enhancement arises from the larger photon–matter interaction and stronger polarization effects in bigger particles, which increases the magnitude of these optical parameters. In contrast, the absorption efficiency (Fig. 7(c)), reflectance, and the imaginary part of the refractive index (Fig. 7(e)). all show a pronounced enhancement with wavelength, indicating stronger photon–matter interactions and more effective electronic transitions. Figure 7 (f) displays the asymmetry parameter (g) of CuO NPs at 50–70 nm as a function of wavelength. The forward scattering effect was enhanced with a positive value of g , and the g value also rose as the NP size grew [60]. Furthermore, for CuO NPs, large values of g indicate light scattering in a narrow wavelength range [61].

4. CONCLUSION

CuO NPs were successfully prepared using the sol-gel method, which involves calcination at 600 °C for 2 h. The XRD pattern confirmed the monoclinic CuO phase and a crystallite size of about 53 nm. The FTIR spectrum verified the chemical bonding of CuO NPs. The TEM investigation confirmed the spherical shape and the rod-like morphology. The spherical particle size was approximately 50–60 nm, while the rod-shaped particles ranged in length from 150 to 200 nm with an average diameter of about 50 nm. The distinct diffraction rings observed in the SAED pattern confirm the polycrystalline structure of the CuO NPs. The binding energies obtained from XPS analysis are associated with the Cu²⁺ and O²⁻ oxidation states. CuO has a direct optical bandgap of 2.0 eV, as shown by the Tauc plot, which is blue-shifted from the bulk value of 1.8 eV. The PL spectra as a function of excitation wavelength revealed that raising the excitation wavelength from 320 nm to 365 nm resulted in enhanced violet emission intensity centered at 428–430 nm and a red shift in peak emission wavelength. The Mie theory–based analysis of the optical properties of CuO NPs in the 50–70 nm size range was employed as a function of wavelength. The calculated results show that spectral efficiencies decrease with increasing wavelength, while the real part of the refractive index decreases and the imaginary part increases, indicating reduced absorption at longer wavelengths. A size-dependent enhancement in optical response is also observed. This may be due to the larger light-matter interaction at larger size. The combined experimental and theoretical results revealed that CuO NPs exhibit tunable optical behavior.

Highlights

- Rod-like CuO NPs was prepared by a facile sol-gel method.
- CuO NPs has monoclinic crystal structure with Cu²⁺ oxidation state.
- Optical band gap is determined from Tauc plot.
- The synthesized NPs possess enhanced visible PL emission.
- The spectral efficiencies and refractive indices were calculated using Mie theory.

IMPRESS

Author contribution

Moges Tsega (Bahir Dar University, Ethiopia) Conceived and designed the experiments; Performed the experiments; Analyzed and interpreted the data; Contributed reagents, materials, analysis tools or data; Wrote the paper.

in Press

Declarations

Conflict of interest

The author declares no competing interests.

In Press

Ethical statement

This article does not contain any studies involving animals or humans.

In Press

Funding statement

This is no funding provided to this research work.

in Press

Acknowledgments

The author would like to thank Prof. F.B Dejene, for his kind cooperation in providing lab synthesis and measurement facilities.

In Press

Table and Figure Captions

Table 1. XRD peak position and calculated structural parameters of CuO NPs.

Fig. 1. The XRD spectrum of CuO NPs after calcined at 600 °C for 2 h.

Fig. 2. FTIR spectrum of CuO NPs.

Fig. 3. (a) Photograph of calcined powder, (b,c) TEM images of the synthesized NPs at different magnifications, (d) SAED pattern CuO NPs.

Fig. 4. (a) XPS survey spectrum, (b) Cu 2p and c O1s core-levels of CuO NPs.

Fig. 5. (a) Diffuse reflectance spectrum, (b) Tauc plot, (c) optical conductivity, (d) Urbach energy of the synthesized CuO NPs.

Fig. 6. PL emission spectra of CuO NPs excited by different wavelength using a 150 W xenon lamp as an excitation source.

Fig. 7. Mie calculations of the (a) extinction efficiency, (b) scattering efficiency, (c) absorption efficiency, (d) real refractive index, (e) imaginary refractive index and (f) asymmetry of CuO NPs for different particle sizes (50–70 nm).

References

- [1] M. S. Chavali, M. P. Nikolova, Metal oxide nanoparticles and their applications in nanotechnology SN. Appl. Sci. 1 (2019) 607.
- [2] H. Sadegh, G. A. M. Ali, V. K. Gupta, A. S. H. Makhlof, R. Shahryarighoshekandi, M.N. Nadagouda, E. Megiel, The role of nanomaterials as effective adsorbents and their applications in wastewater treatment J. Nanostr. Chem. 7 (2017) 1–14.
- [3] N. Beheshtkhoo, M. A. J. Kouhbanani, A. Savardashtaki, A. M. Amani, S. Taghizadeh, Green synthesis of iron oxide nanoparticles by aqueous leaf extract of daphne mezereum as a novel dye removing material, Appl. Phys. A 124 (2018) 363.
- [4] D. Gupta, S. R. Meher, N. Illyaskutty Z. C. Alex, Facile synthesis of Cu₂O and CuO nanoparticles and study of their structural, optical and electronic properties, J. Alloys Compd. 743 (2018) 737.
- [5] H. N. Jayasimha, K. G. Chandrappa, P. F. Sanaula, V. G. Dileepkumar, Green synthesis of CuO nanoparticles: A promising material for photocatalysis and electrochemical sensor, Sens. Int. 5 (2024) 100254.
- [6] N. S. Pavithra, K. N. Manukumar, R. Viswanatha, G. Nagaraju, Combustion-derived CuO nanoparticles: Application studies on lithium-ion battery and photocatalytic activities, Inorg. Chem. Commun. 130 (2021) 108689.
- [7] S. Naz, A. Gul, M. Zia, R. Javed, Synthesis, biomedical applications, and toxicity of CuO nanoparticles, Appl. Microbiol. Biotechnol. 107 (2023) 1039–1061.
- [8] M. Dadkhah, J.-M. Tulliani, Green synthesis of metal oxides semiconductors for gas sensing applications, Sensors, 22 (2022) 4669.
- [9] S. Masudy-Panah, M. Kakran, Y. F. Lim, C. S. Chua, H. Tan, G. K. Dalapatia, Graphene nanoparticle incorporated CuO thin film for solar cell application, J. Renew. Sustain. Energy Rev. 8, 043507 (2016)
- [10] D. R. John, S. Deepapriya, R. M. Cyril, V. P. Annie, M. Jose, D. S. Jerome, Co-precipitation synthesized lanthanum doped copper oxide nanoparticles for supercapacitor applications AIP Conf. Proc. 2244 (2020) 070018.
- [11] I. Abdullahi, S. Hashim, M. I. Sayyed, S. K. Ghoshal, Intense up-conversion luminescence from Dy³⁺ doped multi-component telluroborate glass matrix: Role of CuO nanoparticles embedment, Heliyon, 9 (2023) e15906.
- [12] L. Vimala Devi, T. Selvalakshmi, S. Sellaiyan, P. S. M. kumar, S. Sankar, Combustion derived Y doped CuO nanoparticle: its structural, morphological and optical properties, J. Mater. Sci. Mater. Electron 29 (2018) 9387–9396.
- [13] S. Sagadevan, K. Pal, Z. Z. Chowdhury, Fabrication of CuO nanoparticles for structural, optical and dielectric analysis using chemical precipitation method, J Mater Sci: Mater Electron, 28 (2017) 12591–12597.
- [14] Z. R. Parekh, S. H. Chaki, A. B. Hirpara, G. H. Patel, R. M. Kannaujiya, A. J. Khimani, M. P. Deshpande, CuO nanoparticles—synthesis by wet precipitation technique and its characterization, Phys. B: Condens. 610 (2021) 412950.

- [15] S. K. Misra, S. Nuseibeh, A. Dybowska, D. Berhanu, T. D. Tetley, E. Valsami-Jones, Comparative study using spheres, rods and spindle-shaped nanoplatelets on dispersion stability, dissolution and toxicity of CuO nanomaterials, *Nanotoxicology*, 8 (2014) 422–432.
- [16] L. Dörner, C. Cancellieri, B. Rheingans, M. Walter, R. Kägi, P. Schmutz, M. V. Kovalenko, L. P. H. Jeurgens, Cost-effective sol-gel synthesis of porous CuO nanoparticle aggregates with tunable specific surface area, *Sci. Rep.* 9 (2019) 11758.
- [17] E. Bruno, M. Haris, A. Mohan, M. Senthilkumar, Temperature effect on CuO nanoparticles via facile hydrothermal approach to effective utilization of UV–visible region for photocatalytic activity, *Appl. Phys. A* 127 (2021) 925.
- [18] T. Jiang, Y. Wang, D. Meng, M. Yu, Facile synthesis and photocatalytic performance of self-assembly CuO microspheres, *Superlattice. Microstruct.* 85 (2015) 1–6.
- [19] C. C. Vidyasagar, Y. Arthoba Naik, T. G. Venkatesha, R. Viswanatha, 2012 Solid-State Synthesis and effect of temperature on optical properties of CuO nanoparticles, *Nano-Micro Lett.* 4 (2012) 73–77.
- [20] Z. Alhalili, Green synthesis of copper oxide nanoparticles CuO NPs from eucalyptus globulus leaf extract: Adsorption and design of experiments, *Arab. J. Chem.* 15 (2022) 103739.
- [21] K. Velsankar, V. Vinothini, S. Sudhakar, M. Krishna Kumar, S. Mohandoss, Green synthesis of CuO nanoparticles via *Plectranthus amboinicus* leaves extract with its characterization on structural, morphological, and biological properties, *Appl. Nanosci.* 10 (2020) 3953–3971.
- [22] M. Ahamed, M. J. Akhtar, M. A. M. Khan, H. A. Alhadlaq, Protocatechuic acid mitigates CuO nanoparticles-induced toxicity by strengthening the antioxidant defense system and suppressing apoptosis in liver cells, *J. King Saud Univ. Sci.* 35 (2023) 102585.
- [23] L. Arun, C. Karthikeyan, D. Philip, C. Unni, Optical, magnetic, electrical, and chemo-catalytic properties of bio-synthesized CuO/NiO nanocomposites, *J. Phys. Chem. Solid*, 136 (2020) 109155.
- [24] R. Nithiyavathi, S. J. Sundaram, G. T. Anand, D. R. Kumar, A. D. Raj, D. A. Al Farraj, R. M. Aljowaie, M. R. AbdelGawwad, Y. Samson, K. Kaviyarasu, Gum mediated synthesis and characterization of CuO nanoparticles towards infectious disease-causing antimicrobial resistance microbial pathogens, *J. Infect. Public Health*, 14 (2021) 1893–1902.
- [25] A. L. Patterson, The Scherrer formula for X-ray particle size determination, *Phys. Rev.* 56 (1939) 978–982.
- [26] R. O. Yathisha, Y. Arthoba Nayaka, P. Manjunatha, H. T. Purushothama, M. M. Vinay, K. V. Basavarajappa, Study on the effect of Zn²⁺ doping on optical and electrical properties of CuO nanoparticles, *Phys. E: Low-Dimens. Syst. Nanostructures*, 108 (2019) 257–268.
- [27] K. Athira, L. Gurralla, D. V. R. Kumar, Biosurfactant-mediated biosynthesis of CuO nanoparticles and their antimicrobial activity, *Appl. Nanosci.* 11 (2021) 1447–1457.
- [28] A. M. Eid, A. Fouda, S. E. -D. Hassan, M. F. Hamza, N. K. Alharbi, A. Elkelish, A. Alharthi, W. M. Salem, Plant-based copper oxide nanoparticles; biosynthesis, characterization, antibacterial activity, tanning wastewater treatment, and heavy metals sorption, *Catalysts*, 13 (2023) 348.

- [29] M. Pérez-Alvarez, G. Cadenas-Pliego, O. Pérez-Camacho, V. E. Comparán-Padilla, C. J. Cabello-Alvarado, E. Saucedo-Salazar, Green synthesis of copper nanoparticles using cotton, *Polymers*, 13 (2021) 1906.
- [30] L. Gontrani, E. M. Bauer, A. Talone, M. Missori, P. Imperatori, P. Tagliatesta, M. Carbone, CuO nanoparticles and microaggregates: An experimental and computational study of structure and electronic properties, *Materials*, 16 (2023) 4800.
- [31] S. Bilge, B. Dogan-Topal, E. B. Atici, A. Smaž, S. A. Ozkan, Rod-like CuO nanoparticles/waste masks carbon modified glassy carbon electrode as a voltammetric nanosensor for the sensitive determination of anti-cancer drug pazopanib in biological and pharmaceutical samples, *Sens. Actuators B: Chem.* 343 (2021) 130109.
- [32] M. B. Mobarak, M. S. Hossain, F. Chowdhury, S. Ahmed, Synthesis and characterization of CuO nanoparticles utilizing waste fish scale and exploitation of XRD peak profile analysis for approximating the structural parameters, *Arab. J. Chem.* 15 (2022) 104117.
- [33] M. Maraj, A. Raza, X. Wang, J. Chen, K. N. Riaz, W. Sun, Mo-Doped CuO nanomaterial for photocatalytic degradation of water pollutants under visible light, *Catalysts*, 11 (2021) 1198.
- [34] H. T. Assaouka, D. M. Daawe, R. L. Fomekong, I. N. Nsangou, P. M. Kouotou, Inexpensive and easily replicable precipitation of CuO nanoparticles for low temperature carbon monoxide and toluene catalytic oxidation, *Heliyon*, 8 (2022) e10689.
- [35] A. Klinbumrung, T. Thongtem, S. Thongtem, Characterization and gas sensing properties of CuO synthesized by DC directly applying voltage, *Appl. Surf. Sci.* 313 (2014) 640–646.
- [36] M. A. Khan, N. Nayan, M. K. Ahmad, C. F. Soon, Surface study of CuO nanopetals by advanced nanocharacterization techniques with enhanced optical and catalytic properties, *Nanomaterials*, 10 (2020) 1298.
- [37] A. F. Zedan, A. T. Mohamed, M. S. El-Shal, S. Y. Al-Qaradaw, A. S. AlJaber, Tailoring the reducibility and catalytic activity of CuO nanoparticles for low temperature CO oxidation, *RSC Adv.* 8 (2018) 19499–19511.
- [38] Y. -K. Phang, M. Aminuzzaman, Md. Akhtaruzzaman, G. Muhammad, S. Ogawa, A. Watanabe, L. -H. Tey, Green synthesis and characterization of CuO nanoparticles derived from papaya peel extract for the photocatalytic degradation of palm oil mill effluent (POME), *Sustainability*, 13 (2021) 796.
- [39] X. Xu, M. Zhang, J. Feng, M. Zhang, Shape-controlled synthesis of single-crystalline cupric oxide by microwave heating using an ionic liquid, *Mater. Lett.* 62 (2008) 2787–2790.
- [40] R. Rajamohan, C. J. Raorane, S. -C. Kim, S. Ashokkumar, Y. R. Lee, Novel Microwave Synthesis of copper oxide nanoparticles and appraisal of the antibacterial application, *Micromachines*, 14 (2023) 456.
- [41] E. L. Simmons, Diffuse reflectance spectroscopy: A comparison of the theories, *Appl Opt.* 114 (1975) 1380–1386.
- [42] J. Tauc, R. Grigorovici, A. Vancu, Optical properties and electronic structure of amorphous germanium, *Phys. Status Solidi B*, 15 (1966) 627–637.
- [43] J. Zhao, R. Liu, Z. Hua, Hydrothermal synthesis and optical properties of single crystalline CuO nanosheets, *Superlattices Microstruct.* 81 (2015) 243–247.

- [44] K. Santra, C. K. Sarkar, M. K. Mukherjee, B. Gosh, Copper oxide thin films grown by plasma evaporation method, *Thin Solid Films*, 213 (1992) 226–229.
- [45] P. H. Huh, J. Y. Yang, S. -C. Kim, Facile formation of nanostructured 1D and 2D arrays of CuO islands, *RSC Adv.* 2 (2012) 5491–5494.
- [46] S. N. Rashid, A. S. Jasim, Effect of Nd:YAG laser on the optical properties of nanoparticle CuO solutions, *Mater. Today: Proc.* 80 (2023) 3909–3912.
- [47] D. M. Chethana, T. C. Thanuja, H. M. Mahesh, M. S. Kiruba, A. S. Jose, H. C. Barshilia, J. Manjanna, Synthesis, structural, magnetic and NO₂ gas sensing property of CuO Nanoparticles, *Ceram. Int.* 47 (2021) 10381–10387.
- [48] A. Radhakrishnan, B. B. Beena, Structural and optical absorption analysis of CuO nanoparticles, *Indian J. Adv. Chem. Sci.* 2 (2014) 158–161.
- [49] N. R. Dhineshababu, V. Rajendran, N. Nithyavathy, R. Vetumperumal, Study of structural and optical properties of cupric oxide nanoparticles, *Appl. Nanosci.* 6 (2016) 933–939.
- [50] F. Urbach, The long-wavelength edge of photographic sensitivity and of the electronic absorption of solids, *Phys. Rev.* 92 (1953) 1324.
- [51] A. B. G. Trabelsi, A. M. Mostafa, F. H. Alkallas, W. B. Elsharkawy, A. N. Al-Ahmadi, H. A. Ahmed, S. S. Nafee, R. A. Pashameah, E. A. Mwafy, Effect of CuO nanoparticles on the optical, structural, and electrical properties in the PMMA/PVDF nanocomposite, *Micromachines*, 14 (2023) 1195.
- [52] S. Dagher, Y. Haik, A. I. Ayesh, N. Tit, Synthesis and optical properties of colloidal CuO nanoparticles, *J. Lumin.* 151 (2014) 149–154.
- [53] H. Siddiqui, M. R. Parra, F. Z. Haque, Optimization of process parameters and Its effect on structure and morphology of CuO nanoparticle synthesized via the sol–gel technique, *J. Sol-Gel Sci. Technol.* 87 (2018) 125–135.
- [54] H. Siddiqui, M. S. Qureshi, F. Z. Haque, Surfactant assisted wet chemical synthesis of copper oxide (CuO) nanostructures and their spectroscopic analysis, *Optik*, 127 (2016) 2740–2747.
- [55] M. Ponnar, C. Thangamani, P. Monisha, S. S. Gomathi, K. Pushpanathan, Influence of Ce doping on CuO nanoparticles synthesized by microwave irradiation method, *Appl. Surf. Sci.* 449 (2018) 132–143.
- [56] H. Bahramian, A. Fattah-alhosseini, M. Karbasi, Development of porous ceramic coatings via the PEO process: The key role of CuO nanoparticles in methylene blue photodegradation under visible light illumination, *Appl. Surf. Sci.* 18 (2023) 100511.
- [57] C. F. Bohren, D. R. Huffman, *Absorption and Scattering of Light by Small Particles*, Wiley-Interscience, New York, (1983).
- [58] M. I. Mishchenko, G. Videen, P. Yang, Extinction by a homogeneous spherical particle in an absorbing medium, *Opt. Lett.* 42 (2017) 4873–4876.
- [59] P. F. Liaparinos I. Kandarakis, The imaging performance of compact Lu₂O₃:Eu powdered phosphor screens: Monte Carlo simulation for applications in mammography, *Med. Phys.* 36 (2009) 1985–1997.

- [60] P. F. Liaparinos, Strain effects on the optical parameters of quantum dots nanocrystals employed in biomedical applications, *J. Lumin.* 146 (2014) 193–198.
- [61] K. Ehler, H. Moosmüller, Small and large particle limits of the asymmetry parameter for homogeneous, spherical particles, *Aerosol Sci. Technol.* 57 (2023) 425–433.

ImPress

Table 1. XRD peak position and calculated structural parameters of CuO NPs.

Miller indices (<i>hkl</i>)	2 θ	FWHM	<i>d</i> -spacing (Å)	Lattice constants (Å)			Unit cell Volume (Å ³)	Average crystallite size (nm)	Average micro-strain	Dislocation density (m ⁻²)	Urbach energy (eV)
				<i>a</i>	<i>b</i>	<i>c</i>					
(002)	35.3	0.1574	2.5275	4.6336	3.4296	5.1251	80.33	53	8.3×10 ⁻³	3.6×10 ¹⁴	0.84
(111)	38.57	0.1574	2.3168								
(-202)	48.5	0.2558	1.8718								

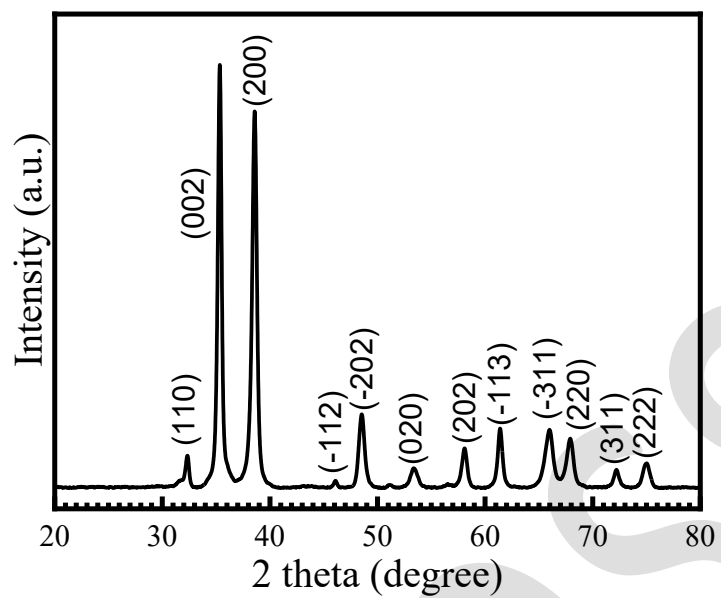


Fig. 1. The XRD spectrum of CuO NPs after calcined at 600 °C for 2 h.

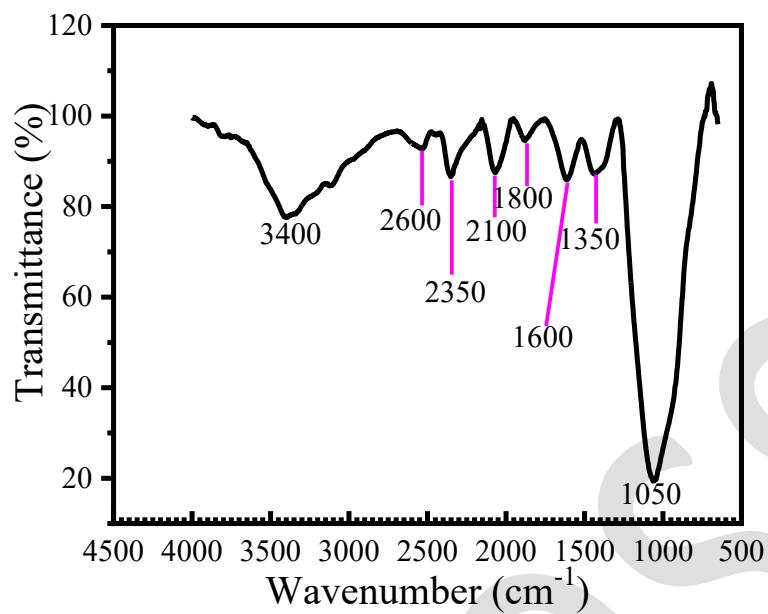


Fig. 2. FTIR spectrum of CuO NPs.

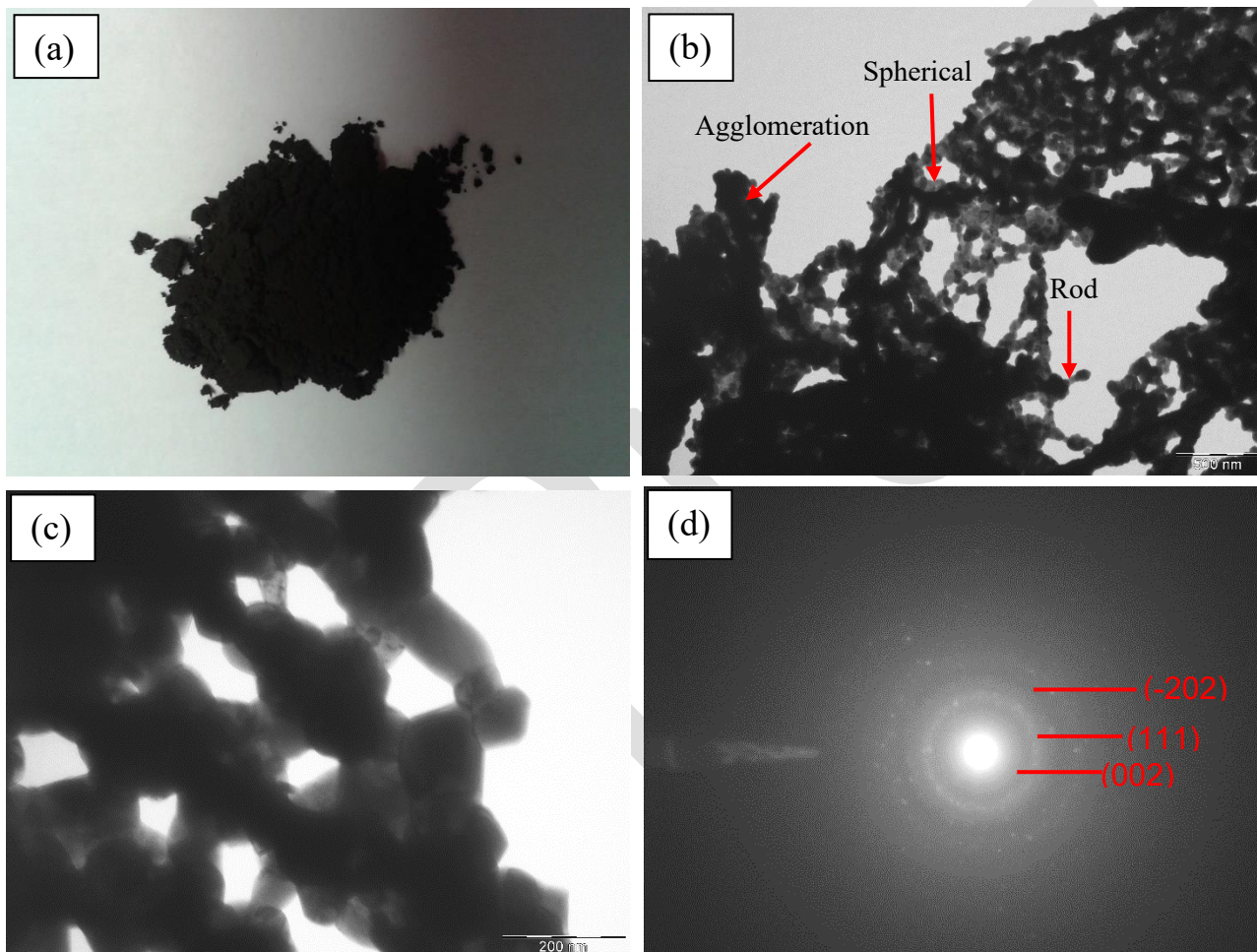


Fig. 3. (a) Photograph of calcined powder, (b,c) TEM images of the synthesized NPs at different magnifications, (d) SAED pattern CuO NPs.

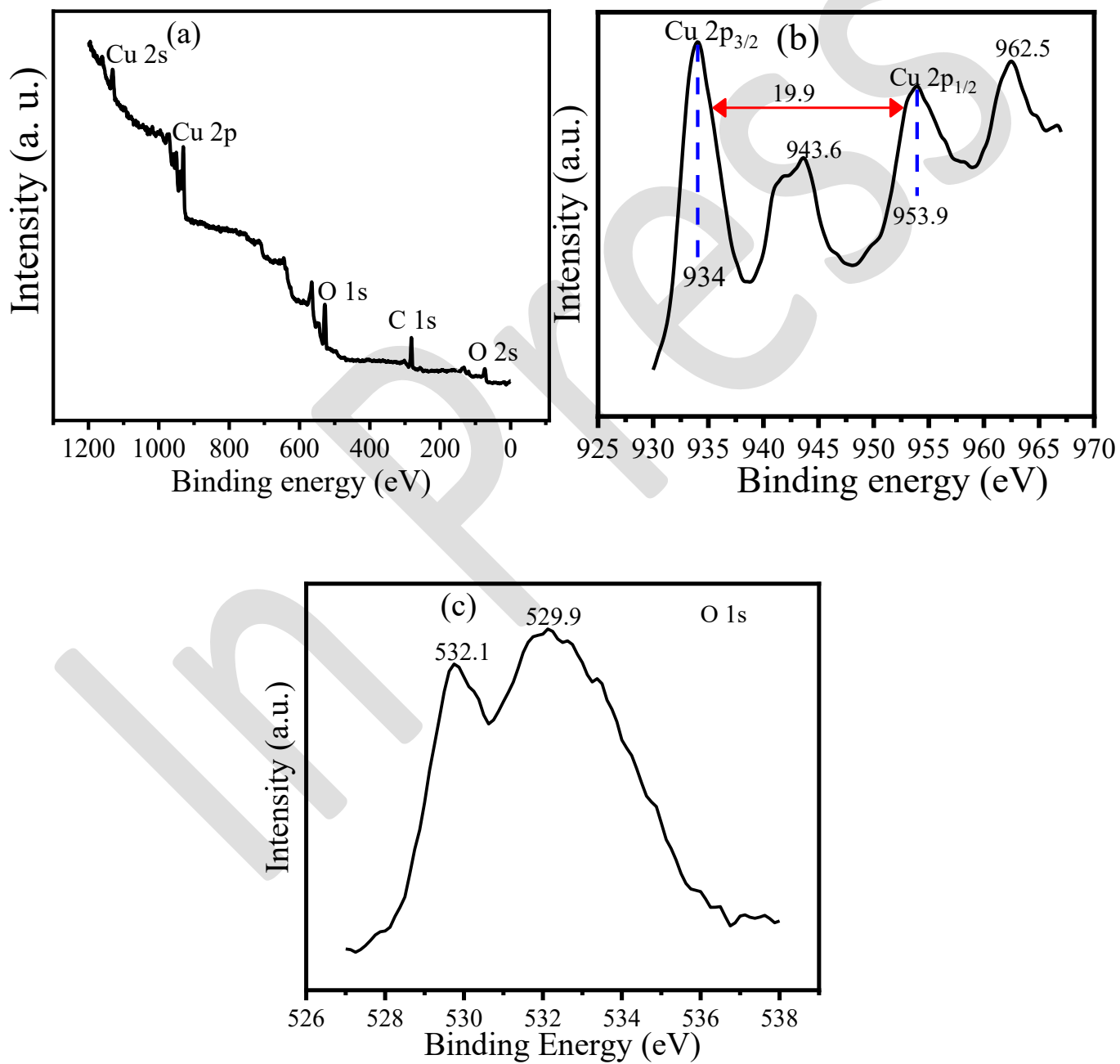


Fig. 4. (a) XPS survey spectrum, (b) Cu 2p, (c) O1s core-levels of CuO NPs.

In Press

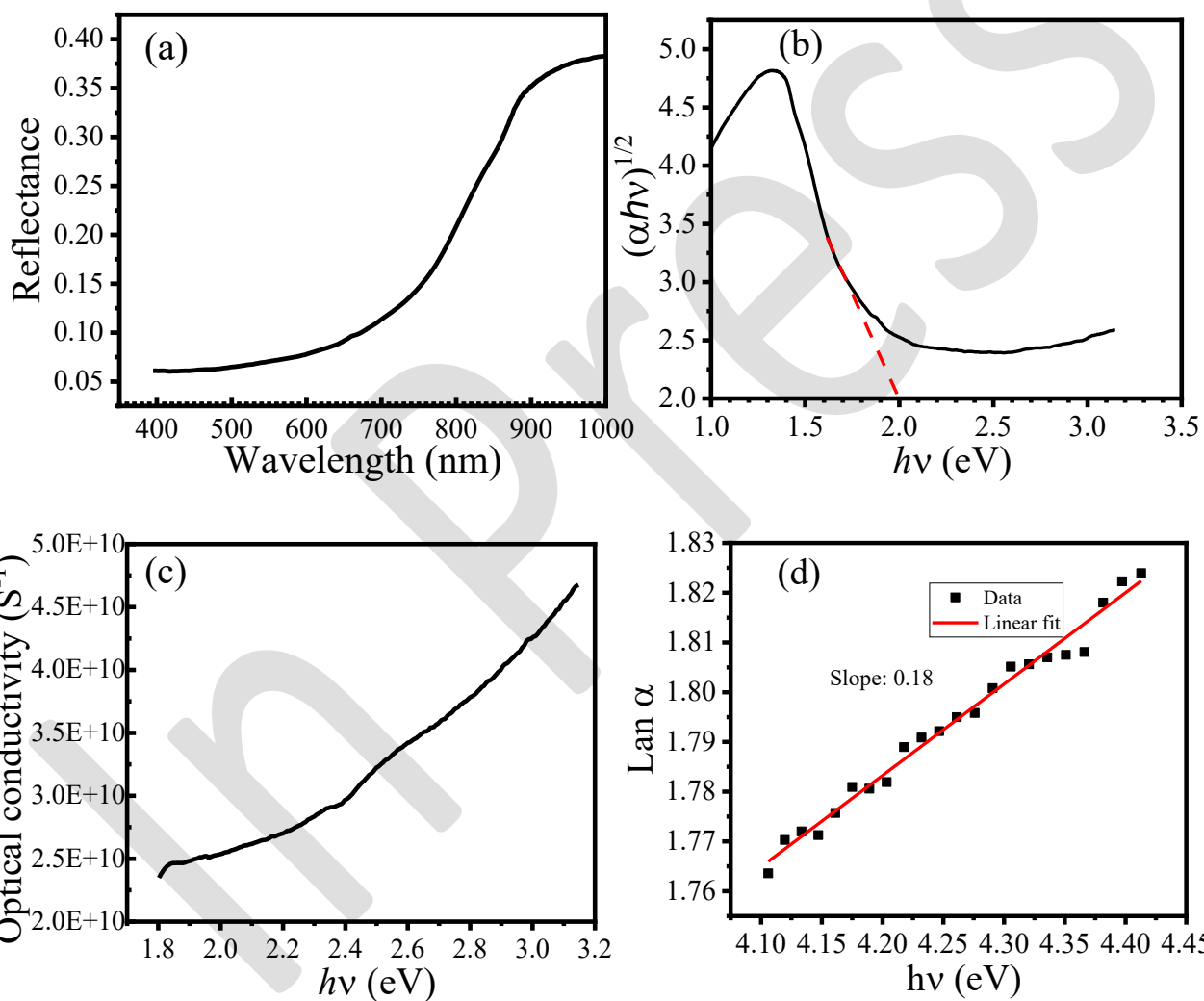


Fig. 5. (a) Diffuse reflectance spectrum, (b) Tauc plot, (c) optical conductivity, (d) Urbach energy of the synthesized CuO NPs.

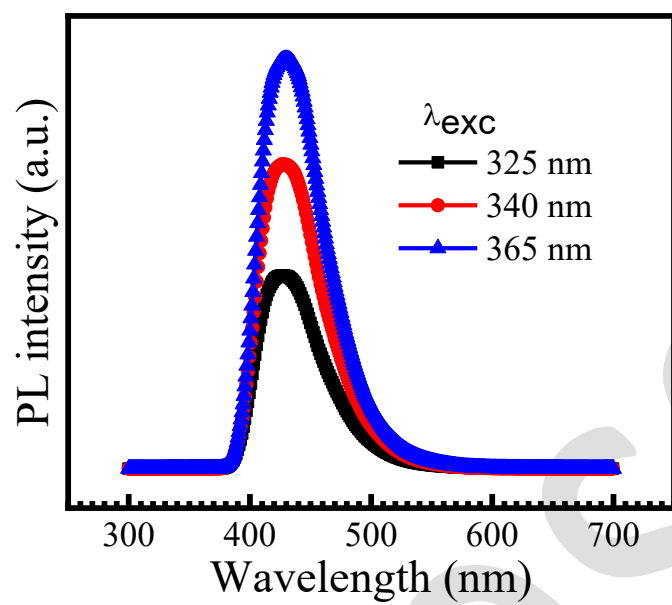


Fig. 6. PL emission spectra of CuO NPs excited by different wavelength using a 150 W xenon lamp as an excitation source.

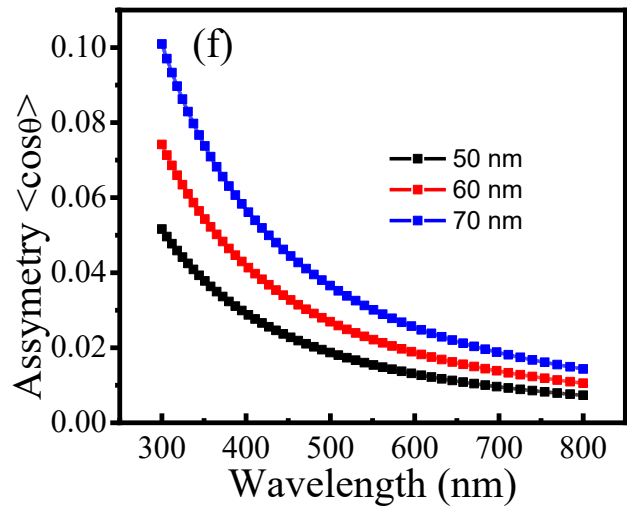
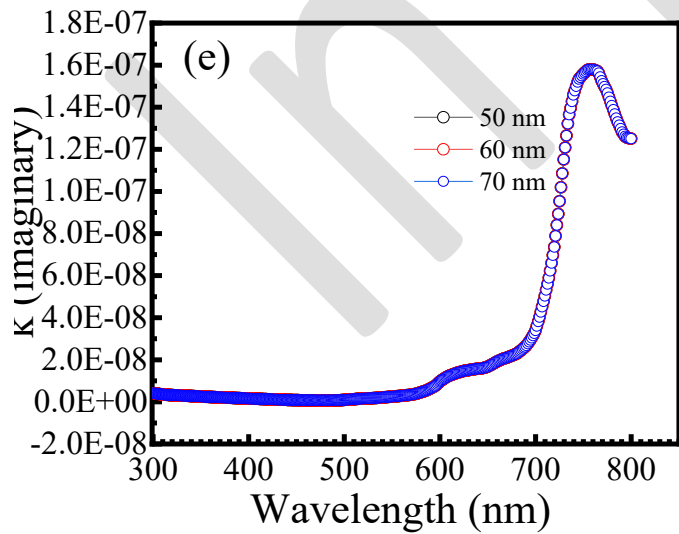
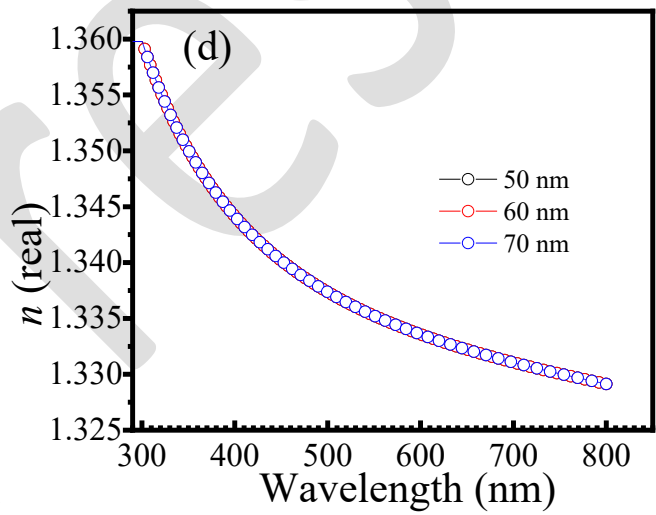
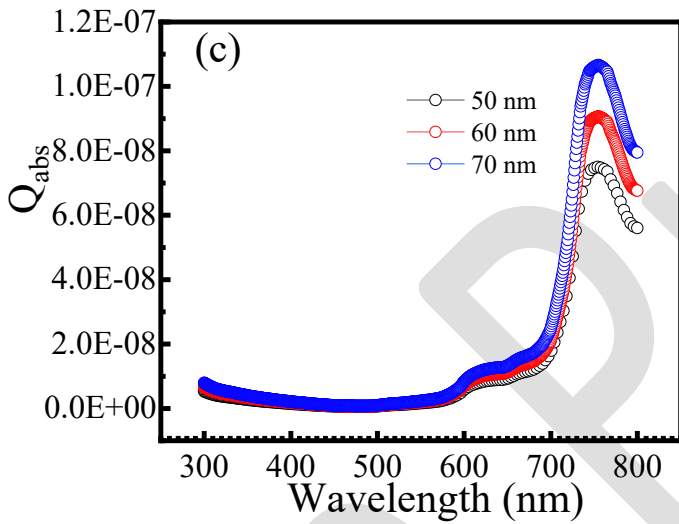
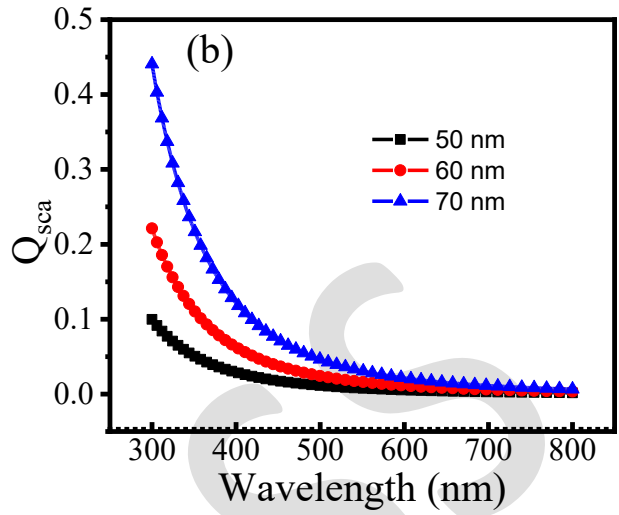
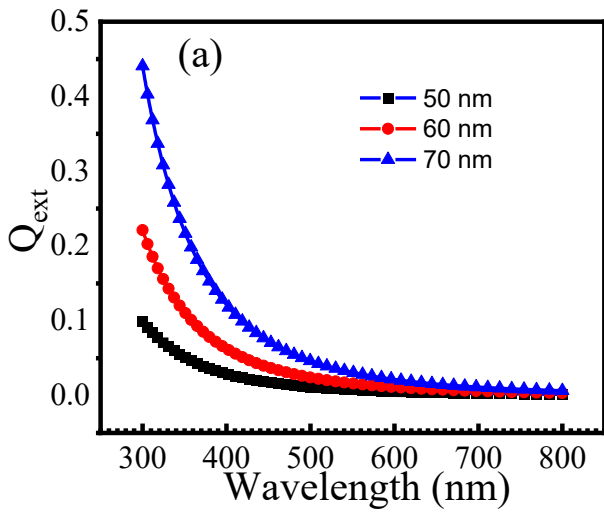


Fig. 7. Mie calculations of the (a) extinction efficiency, (b) scattering efficiency, (c) absorption efficiency, (d) real refractive index, (e) imaginary refractive index and (f) asymmetry of CuO NPs for different particle sizes (50–70 nm).

in Press